Smart Structures and Systems, *Vol. 13, No. 2 (2014) 281-303*
DOI: http://dx.doi.org/10.12989/sss.2014.13.2.281

Active mass driver control system for suppressing wind-induced vibration of the Canton Tower

Huai-bing Xu[**1], Chun-wei Zhang[1], Hui Li[1], Ping Tan[2], Jin-ping Ou[*1] and Fu-lin Zhou[2]

[1]*School of Civil Engineering, Harbin Institute of Technology, Harbin 150090, China*
[2]*The State Key Laboratory of Seismic Reduction/Control & Structural Safety (Cultivation), Guangzhou University, Guangzhou 510405, China*

(Received August 8, 2012, Revised November 4, 2013, Accepted November 23, 2013)

Abstract. In order to suppress the wind-induced vibrations of the Canton Tower, a pair of active mass driver (AMD) systems has been installed on the top of the main structure. The structural principal directions in which the bending modes of the structure are uncoupled are proposed and verified based on the orthogonal projection approach. For the vibration control design in the principal X direction, the simplified model of the structure is developed based on the finite element model and modified according to the field measurements under wind excitations. The AMD system driven by permanent magnet synchronous linear motors are adopted. The dynamical models of the AMD subsystems are determined according to the open-loop test results by using nonlinear least square fitting method. The continuous variable gain feedback (VGF) control strategy is adopted to make the AMD system adaptive to the variation in the intensity of wind excitations. Finally, the field tests of free vibration control are carried out. The field test results of AMD control show that the damping ratio of the first vibration mode increases up to 11 times of the original value without control.

Keywords: structural vibration control; variable gain feedback control; wind-induced vibration; active mass driver; linear motor

1. Introduction

Structural control has already been recognized as an efficient approach to suppress the vibration of structures due to external excitations. Since Yao (1972) introduced the theory of modern control into civil engineering, various control strategies and systems have been extensively studied in theory and in practice (Housner *et al*. 1997, Ou 2003). In 1989, the first full-scale active control system was applied to an office building in Tokyo (Ikeda *et al*. 2001). This application promoted the development of active structural control systems. From then on, tens of active control systems have been implemented into high-rise buildings and bridge towers. Most of the applied AMD systems are driven by servo hydraulic actuators or motors (Spencer and Nagarajaiah 2003,

∗Corresponding author, Professor, E-mail: oujinping@hit.edu.cn
**Co-corresponding author, E-mail: xuhuaibing07@126.com

http://www.techno-press.org/?journal=sss&subpage=8 ISSN: 1738-1584 (Print), 1738-1991 (Online)

Yamamoto *et al*. 2001, Fujita 2002). Recently, a set of two identical active tuned mass dampers were installed on the top of Shanghai World Financial Center Tower to mitigate the wind-induced vibration. The active driving devices are the rotating motors with ball screws. The analysis and field measurement results show that the active tuned mass dampers increased the damping ratio up to eight times and reduced the wind-induced acceleration response up to 60% (Lu *et al*. 2012).

For the control of wind-induced vibrations of high-rise structures, the first order mode usually dominates in the response of the building's top on which an AMD system is usually placed, and consequently the dominant frequency of optimal control force is usually close to the fundamental frequency of the objective structure. Then if the fundamental period of the objective structure is long, the dominant period of the active control force would be long accordingly, which makes the mass stroke requirement of the AMD system be significantly big. The period of the first order mode of the objective structure in this paper is about 11 seconds. According to the capacity of auxiliary mass and the objective control effectiveness as designed, the stroke requirement of the AMD system is about 1.4 meters. This is a significant stroke requirement for hydraulic actuators or rotary motors. The greater the capacity of the actuator is, the bigger the necessary size of piston or ball screws will be required (Nakamura 2001), which may introduce problems such as compression stability, loud noise, big friction, etc.

To meet the challenge in choosing appropriate actuator for the low frequency AMD control system, there are some advantages in utilizing linear motor as the driving device of the long stroke actuator. The stroke of linear motor primarily depends on the length of the stator which can be fabricated specifically as long as required. The friction of linear motor driver is relatively small because there is no transmission device coupling rotary motion with linear motion of the inertia mass. Without compression components, like pistons in hydraulic actuators or ball screws in rotational motors, the compression stability problem can be avoided by linear motor drivers. As a result, a compact, smooth and long stroke AMD system and good vibration-control performance can be realized. Two sets of hybrid mass dampers driven by cylindrical linear-induction servomotors were installed in a 21-storey building in Oita City, Japan (Nakamura 2001). A hybrid mass damper system driven by a linear actuator was applied to a 36-storey high-rise building in Tokyo (Nagashima 2001).

In former investigations and implementations of AMD control, constant gain feedback control strategies, such as direct acceleration feedback, direct velocity feedback, LQ optimal control and Hinf control, are usually adopted. However, the constant gain feedback control lacks adaptivity to the variation of the intensity level of the wind excitations, i.e., under stronger wind excitations, the stroke of AMD may exceed the stroke limitation; under weaker wind excitations, the capacity of the AMD system cannot work efficiently (Nagashima 1997). Bhartia *et al*. (1993) and Indrawan *et al*. (1994) adopted bang-bang control algorithm to solve the saturation problem of the control force. Fujita et al. (1992) adopted a set of switchable gains to protect the AMD against strong earthquakes and strong winds. The AMD stroke was kept within the strong limit of the hydraulic actuators. However, Nagashima and Shinozaki (1997) pointed out that frequent discontinuous switching control may cause chattering and performance deterioration. They proposed a continuously variable gain feedback (VGF) control strategy to satisfy the constraints of the AMD system.

This paper introduces the vibration control of Canton tower with an AMD system. The structural principal directions of bending modes are analyzed and verified with measured response. The full scale AMD system driven by linear motors is introduced and certified with test results. Continuously variable gain feedback control strategy considering the AMD stroke constraints is

studied to adapt the intensity variation of wind excitations. Field tests of free vibration control are conducted to certify the effectiveness of the AMD system.

2. Dynamical properties of the Canton Tower structure

The Canton Tower, which used to be named as the Guangzhou New TV Tower, is a tower used for broadcasting and sightseeing. The height of the tower is 600 m, which consists of a 450 m high main tower and a 150 m high antenna. The total weight of the building is about 1.94×10^5 ton. The main tower is a shear-flexural structure, composed of inner reinforced-concrete (RC) core tube and the steel frame outside, where the steel frame is composed of inclining columns of concrete filled steel tubes, steel ring beams and steel braces (Fig. 1(a)).The tower is so slender, with long natural period and low damping, that it is very sensitive to wind excitations. Moreover, the tower locates in Guangzhou, on the coastline of the South China Sea, where strong winds and typhoons occur frequently every year. Therefore, studying the vibration control of the tower is remarkably significant.

2.1 Principal directions of bending modes

The tower has been established as an international benchmark problem for structural health monitoring (SHM) studies by the Hong Kong Polytechnic University (PolyU) (Ni *et al*. 2009, 2011). The SHM system has been implemented on the tower. The accelerometer positions and measurement directions are shown in Fig. 1(a). A total of 20 uni-axial accelerometers were installed at eight levels. The 4th level and the 8th level were equipped with four uni-axial accelerometers, two for measurement of the horizontal acceleration along the long-axis of the inner core tube, and the other two for the short-axis of the inner core tube. At the other six levels, each section was equipped with two uni-axial accelerometers, one along the long-axis and the other along the short-axis. The sampling frequency of the acceleration and wind data was set to 50 Hz. Many researchers have studied the modal identification methods under ambient excitation based on the benchmark problem (Chen *et al*. 2012, Chung *et al*. 2012). A special issue on the benchmark problem has been published on the journal of Smart Structures and Systems Vol. 10, No. 4-5.

In the SHM benchmark problem, the two orthogonal directions of the sensors were placed along the short-axis and the long-axis of the inner core tube, respectively. Chen *et al*. (2012) analyzed the dynamical properties of the tower based on the ambient vibration measurements. The frequencies and the mode shapes of the tower were obtained. As given in the Fig. 4 in Chen *et al*. (2012), however, the short-axis components and long-axis components of the bending mode shapes are coupled.

Modal analysis of the finite element structure model shows that, the included angle between the principal direction of the bending modes and the short-axis direction of the inner core tube is about 16°. The principal directions of the bending modes are symbolled as principal X direction and principal Y direction, respectively (as shown in Fig. 1(b)). Then the acceleration measurements in the SHM benchmark problem are transformed into the two principal directions based on the orthogonal projection approach:

$$\begin{aligned} A_{px}[i] &= A\left[Ch(1,i)\right]\cos(\theta) + A\left[Ch(2,i)\right]\sin(\theta) \\ A_{py}[i] &= -A\left[Ch(1,i)\right]\sin(\theta) + A\left[Ch(2,i)\right]\cos(\theta) \end{aligned} \quad (i = 1,2,\cdots,10) \tag{1}$$

Where Ch is the array of the channel numbers as given in Fig. 1(a)

$$Ch = \begin{bmatrix} 1 & 3 & 5 & 7 & 8 & 11 & 13 & 15 & 17 & 18 \\ 2 & 4 & 6 & 10 & 9 & 12 & 14 & 16 & 20 & 19 \end{bmatrix}$$

The channels of $Ch(1,i)$ are along the short-axis direction of the inner core tube, while $Ch(2,i)$ are along the long-axis direction of the inner core tube. $A[k](k = 1,2,\cdots,20)$ is the measured acceleration result of the k th channel in the coordinate of the SHM benchmark problem. $A_{px}[i]$ and $A_{py}[i]$ are the orthogonal projection of $A\left[Ch(1,i)\right]$ and $A\left[Ch(2,i)\right]$ in the principal direction of the bending modes. $\theta = 16^{\circ}$ is the included angle between the principal direction of the bending modes and the short-axis direction of the inner core tube.

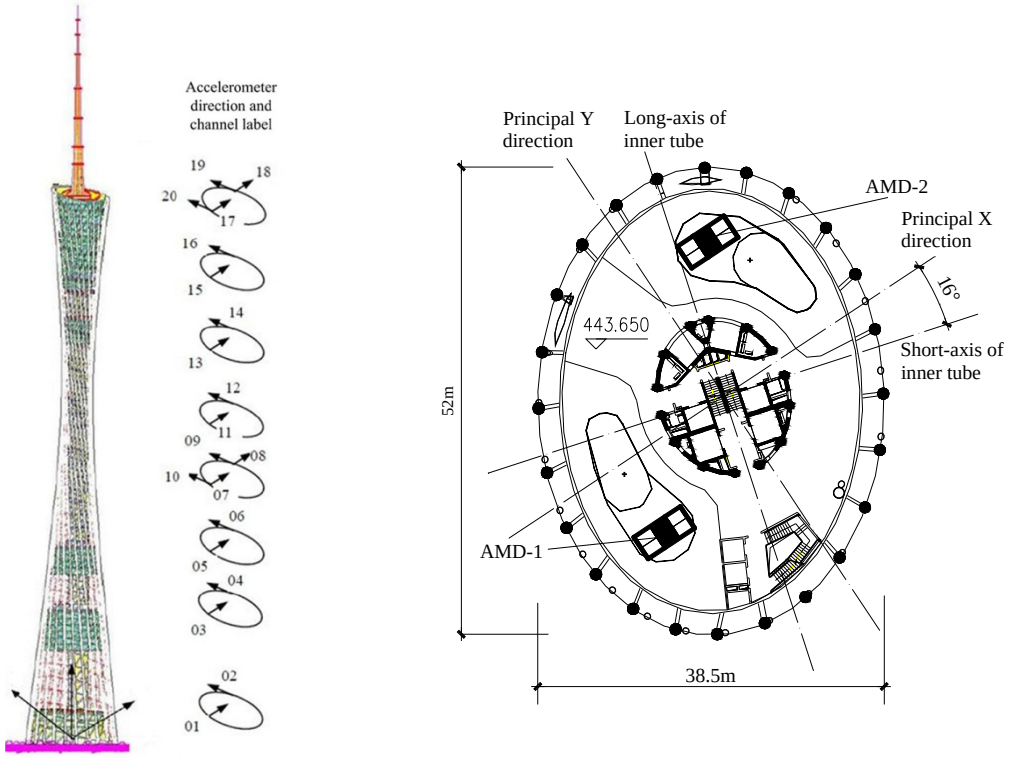

(a) (b)

Fig. 1 Accelerometer direction for SHM system and the principal direction: (a) Placement and direction of accelerometers for SHM system (Fig. 1(a) in Chen *et al*. (2012)) and (b) Principal directions for AMD control

The same data as used in Chen *et al*. (2012) is adopted to verify the principal direction. That is the measurements recorded from 19:00 pm to 20:00 pm on 19 January 2010 with the SHM system. The accelerations in the principal directions are obtained though orthogonal projection approach. Fig. 2 shows the power spectrum density (PSD) of the accelerations. Fig. 2(a) shows that the accelerations along the short-axis / long-axis directions of the inner core tube, as adopted in the SHM benchmark problem, are coupled. While Fig. 2(b) indicates that the orthogonal projection in the principal directions of the bending modes are uncoupled. The frequency range in Fig. 2(b) is 0 ~ 1.6 Hz which includes the first five modes in the principal X direction, the first five modes in the principal Y direction and the first two modes of torsional modes. The two vibration mode with the frequencies of 0.5051 Hz and 1.25 Hz are the first two torsional vibration modes, respectively. The amplitudes of the PSD peaks show that the vibration in principal X direction is much more dominative than those in principal Y direction and torsional direction. The amplitude of the accelerations in principal X direction is about more than 2 times of that in principal Y direction. In this study, only the vibration in principal X direction is controlled. Fig. 3 shows the stabilization diagram of the orthogonal projections in the principal directions used for the stochastic subspace identification (SSI) technique. The identified modal frequencies using SSI technique agree well with the PSD results. Table 1 lists the frequencies identified and Fig. 4 implies that the mode shapes in principal directions are almost uncoupled.

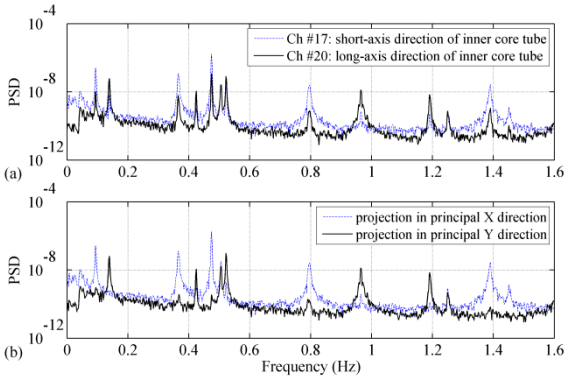

Fig. 2 Power spectrum density of the accelerations under ambient excitation: (a) Measured acceleration results along the directions in SHM benchmark problem and (b) Orthogonal projection of accelerations to the principal directions of the bending modes

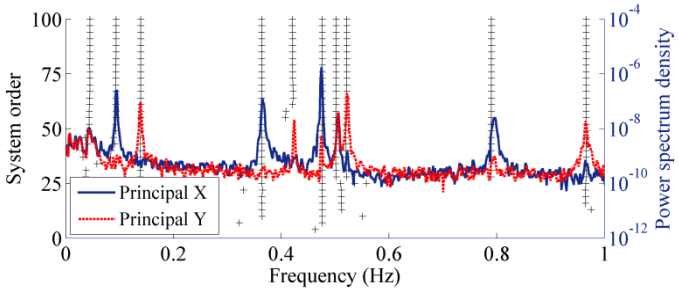

Fig. 3 Stabilization diagram of frequencies

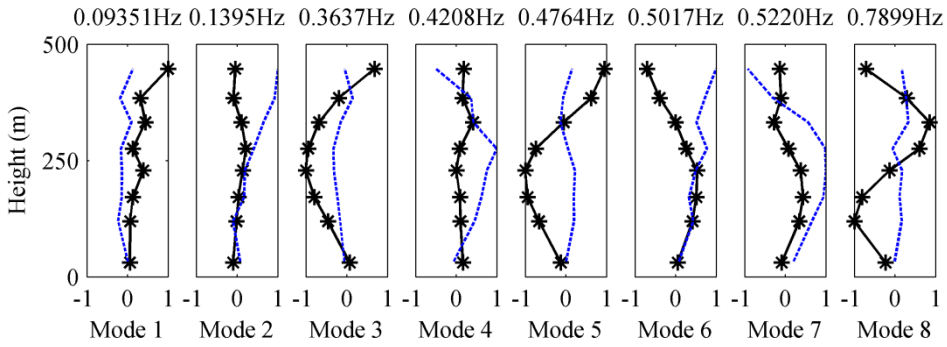

Fig. 4 Mode shapes in principal directions: Solid line with *----principal X; Dot line----principal Y

Table 1 Frequencies identified with SSI technique

Mode	Frequencies identified (Hz)	Mode description
1	0.0935	Principal X bending
2	0.1395	Principal Y bending
3	0.3637	Principal X bending
4	0.4208	Principal Y bending
5	0.4764	Principal X bending
6	0.5017	Torsion
7	0.5220	Principal Y bending
8	0.7899	Principal X bending

2.2 Feedback subsystem for AMD control

A feedback subsystem is installed on the structure to measure the structural responses for AMD controller. It is noted that the directions of the sensors for vibration control system are not along the same directions as that of the sensors for SHM system. The sensors used in feedback subsystem are along the principal X direction. The feedback system consists of sensors, transmissions and data acquisition devices (Fig. 5).

Multiple sensors, such as accelerometers and velocity transducers, are installed on the structure to feedback the vibration of the structure, as shown in Fig. 6 and Table 2. As the structure is very slender, the sensors adopted must have good low-frequency characteristics and high sensitivities. The frequency range of the sensors is 0 (DC) ~ 100 Hz. The sensitivities of accelerometers and velocity transducers are about 5 mV/gal and 5 V/(m/s) respectively. The sensors are placed at the heights of 168 m, 227 m, 386 m, 438 m and 529 m. The controller of AMD is positioned on the floor with a height of 438 m. As the transmission distance is too long from the sensors to the controller, optical fibers are adopted to transmit the signals instead of metal wires which would make the signals decay significantly.

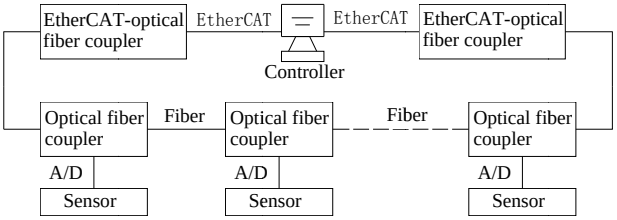

Fig. 5 Feedback subsystem for AMD control system

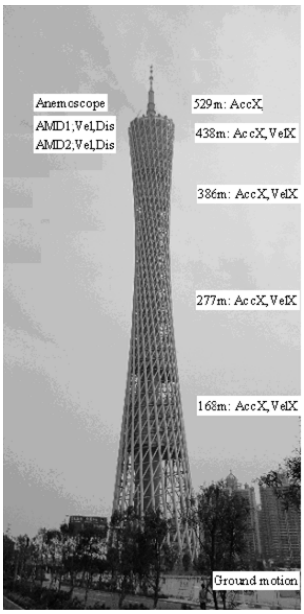

Fig. 6 Sensors for structural control

2.3 Simplified structural model for vibration control

The size of the 3D finite element model is too large for structural control analysis and application. To reduce the analytical effort, the tower is discretized to a 53 degree-of-freedom (DOF) lumped mass model. The main tower consists of 39 lumped mass nodes while the mast is modeled with 14 nodes. Each concentrated mass node has a lateral DOF along principal X direction. The location of the two AMD control systems both correspond to the 37th DOF. The mass matrix $\mathbf{M}_s$ and stiffness matrix $\mathbf{K}_s$, are obtained based on the three-dimensional finite element model established in ANSYS. The mass matrix $\mathbf{M}_s$ is a diagonal matrix, while the stiffness matrix $\mathbf{K}_s$ is a full matrix.

After construction completion, the accelerations and velocities of the structure are measured under wind excitations. The sampling frequency is 50 Hz and the duration is 2 hours. The modal properties, such as the frequencies and mode shapes are identified through power spectrum analyses. The original 53-DOF model is modified according to the measured results of the

frequencies and the mode shapes of the first 5 modes in principal X direction. As the stiffness matrix $\mathbf{K}_s$ is a full matrix, only the mass matrix $\mathbf{M}_s$ is modified in this paper. Table 3 and Fig. 7 indicate that dynamic properties of the modified model agree well with the measured results. The modified 53-DOF model can be used for the design and analysis of structural vibration control.

The damping ratio of mode X1 is measured through forced vibration tests with AMD as an actuator. The measured acceleration at the height of 438 m is shown in Fig. 21(a). The damping ratio of the X1 mode is calculated to be 0.35 percent with the logarithmic decrement. The damping ratio of the X2 mode is identified to be about 1 percent with the SSI technique based on the measurements under wind excitations. The Rayleigh damping matrix $\mathbf{C}_s$ is constructed according to these damping ratios.

Table 2 Sensors for AMD control

No.	Location	Type
1	168m	Velocity
2	168m	Acceleration
3	277m	Velocity
4	277m	Acceleration
5	386m	Velocity
6	386m	Acceleration
7	438m	Velocity
8	438m	Acceleration
9	529m	Acceleration
10	AMD-1	Relative displacement
11	AMD-1	Relative velocity
12	AMD-2	Relative displacement
13	AMD-2	Relative velocity

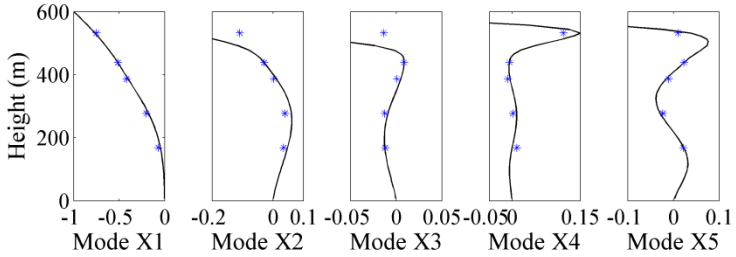

Fig. 7 Mode shapes in principal X direction of the modified model compared with the identified results: Solid line ---- mode shapes of the modified 53-DOF model; * ---- mode shapes identified based on field measurements

Table 3 Natural periods of the modified model

Mode	Natural period (s)			Relative error (%)
	FE model	Measured	Modified model	
X1	9.9615	11.1074	11.1472	0.3583
X2	2.8927	2.7196	2.7403	0.7611
X3	2.2744	2.1631	2.1901	1.2476
X4	1.4276	1.7361	1.5836	-8.7813
X5	0.9959	1.2483	1.1816	-5.3433

Note: The mode X4 is the bending mode of the mast. More sensors will be installed at the height of 578 m in the update of the system to enhance the accuracy of the measurements.

3. AMD control system

Based on the above results, the tower mainly vibrates in the translational direction, especially in principal X direction. A set of two AMD control subsystems is installed in the top of the main tower to suppress the vibration in principal X direction (Fig. 1(b)). As illustrated in Fig. 1(b), the AMD system consists of two AMD subsystems, AMD-1 and AMD-2. The two AMD subsystems are installed on two water tanks, at the opposite sides of the RC core tube along the principal X direction. The two tanks are assumed to be fixed on the floor in this study, although they can be used as the inertia mass of tuned mass dampers in other studies.

3.1 Linear motor actuator based AMD system

The AMD subsystems are driven by permanent magnet synchronous linear motors. The basic principle of permanent magnet synchronous linear motor is that the magnetic field exerts ampere force to the live conductor in it. When the windings in the magnetic field are live, the ampere force will drive the mover moving along the linear guides (Hellinger *et al*. 2009). The schematic of the AMD driven by a linear motor is shown in Fig. 8(a). The linear motor mainly consists of linear motor stator (rows of permanent magnet blocks), linear motor mover (3-phase windings), linear guides and system chassis. The auxiliary mass is fixed to the linear motor mover, and they both constitute the moving inertia mass of AMD subsystem. The linear motor stator, linear guides and base are fixed to the structure floor.

The AMD system driven by a linear motor has the following features: (1) long stroke which only depends on the length of the stator and the linear guides adopted; (2) fast action and small time-delay as the thrust force is generated through the rapidly regulated current; (3) low friction and high reliability because of the simple mechanical transmission and low wearing rates; (4) small space demanded because of the system constitution is simple and compact.

The AMD system adopted in the Canton Tower is shown in Figs. 8(b) and 9. The stator of linear motor is composed of two rows of permanent magnets. The auxiliary inertia mass, with an overall dimension of 2.2 m (length), 2.9 m (width) and 1.15 m (height), is composed of steel blocks. The inertia mass is supported by three rolling linear guides with the length of 6 m.

Hydraulic bumpers are installed at the ends of linear guides to prevent inertia mass from impacting the structure. The controller of AMD system is an industrial PC, with real-time software environment TwinCAT®. Power amplifier, water cooling device and feedback system are also integrated into the AMD system. The main parameters of each AMD subsystem are listed in Table 4.

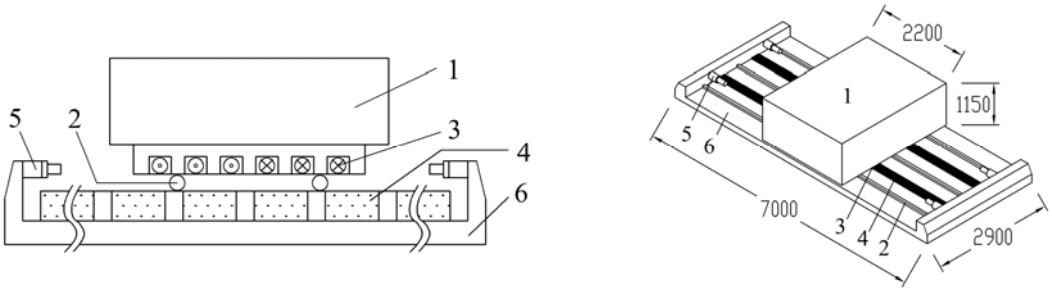

(a) Schematic of the AMD system (b) 3D model of the AMD system

Fig. 8 Schematics of the AMD system driven by a linear motor: 1-auxilary inertia mass; 2- linear guides; 3- three-phase windings; 4- permanent magnets; 5- bumper; 6- system chassis

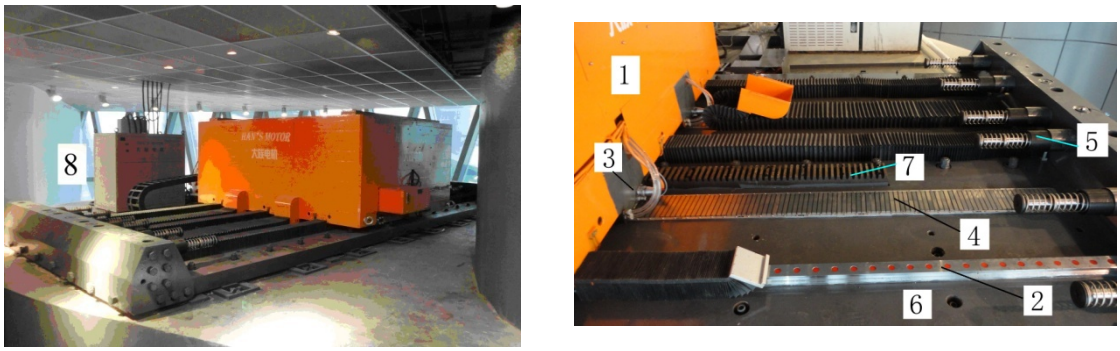

(a) Over view (b) Composition

Fig. 9 AMD system adopted in Canton Tower: 1~6- refer to annotations in Fig. 8; 7- lock-out system; 8- linear motor driver (power amplifier)

3.2 Dynamic model of AMD system

Open-loop tests are carried out to obtain the dynamic performance of the AMD system. The schematic of the open-loop tests is shown in Fig. 10. F_c is the target driving force command; V is the command voltage to the motor driver; i_{drv} is the circuit current that drives the linear motor; d and v are the relative displacement and relative velocity of the AMD inertia mass with respect

to the fixed base; d is measured with an optical grating scale sensor; v is fed back from the linear motor driver. In addition, the acceleration of the AMD inertia mass a is also measured by using an accelerometer. To confirm the short time delay of the system, the sampling rate of open-loop tests is set to be 1000 Hz.

The open-loop tests include step force testing and sinusoidal force testing. The amplitude of the force command ranges from 1.2 kN to 30 kN. The sinusoidal frequencies cover 0.05 Hz, 0.1 Hz, 0.15 Hz, 0.5 Hz, 1 Hz and 2 Hz. In open-loop tests, both the target force command and the actual driving force are recorded synchronously. The time delay of control force is verified to be less than 10 ms (Fig. 11), regardless of the amplitude or the frequency of the command force. The time delay is so far smaller than the dominant periods (1.25 s ~ 11.1 s) of the structure that the time delay is considered to be small enough to have low impact on system performance. So the time delay is ignored in the dynamic performance analysis and the following AMD control tests.

Table 4 Specification of each AMD subsystem

Items	Value
Moving inertia mass (ton)	~56
Effectiveness mass ratio	0.12%
Maximum travel (m)	±1.4
Maximum velocity (m/s)	0.5
Rated thrust (kN)	30
Peak thrust (kN)	60
Rated power (kW)	15

The equation of motion of the AMD subsystem can be represented as

$$F_a + F_f + F_s = m_a a \tag{2}$$

where F_a is the actual driving force of the linear motor; F_f is the resistance force from the linear bearings; F_s is the constant force induced by the inclination of the linear guides. As the friction force of the AMD system driven by linear motor is usually very small, the resistance force F_f can be approximated as a viscous force by introducing an equivalent viscous coefficient c_{eq}, i.e., $F_f = -c_{eq} v$.

Then the equation of motion can be rewritten as

$$F_a - c_{eq} v + F_s = m_a a \tag{3}$$

$$\dot{v} + \frac{c_{eq}}{m_a} v = \frac{1}{m_a}\left(F_a + F_s\right) \tag{4}$$

For step force cases, Eq. (4) is an one-order linear differential equation with constant coefficients. The analytical solution of the velocity v and displacement d can be derived.

$$v = \frac{F_a + F_s}{c_{eq}}\left(1 - e^{-\frac{c_{eq}}{m_a}t}\right) \tag{5}$$

$$d = \frac{m_a\left(F_a + F_s\right)}{c_{eq}^2}\left(e^{-\frac{c_{eq}}{m_a}t} + \frac{c_{eq}}{m_a}t - 1\right) \tag{6}$$

where m_a, c_{eq} and F_s are constant coefficients to be determined. The estimate of m_a is about 56 ton. Through the open-loop tests of step force cases, a series of time-history records of actual driving force F_a, velocity v, displacement d with respect to time t can be acquired. According to these time-history records, coefficients m_a, c_{eq} and F_s can be determined based on nonlinear least-square fitting method. Table 5 lists the fitting results of the coefficients, where the resistance in AMD-2 is shown to be much bigger than that in AMD-1 due to the defective installation.

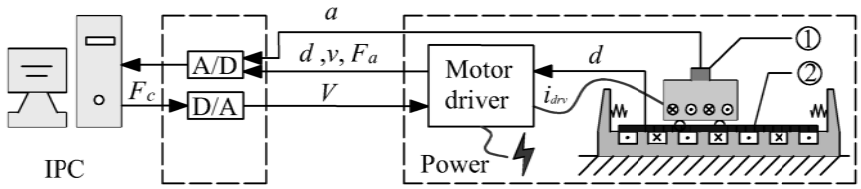

Fig. 10 Schematic of experiment system: 1- accelerometer; 2- optical grating scale sensor

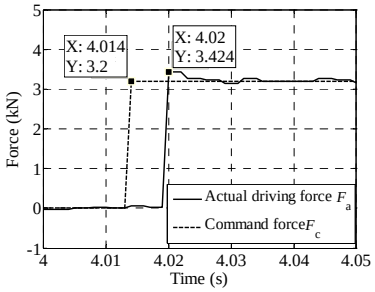

(a) Step force case (3.2 kN)

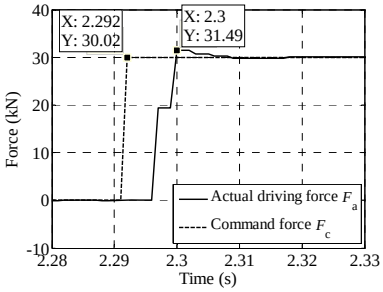

(b) Step force case (30 kN)

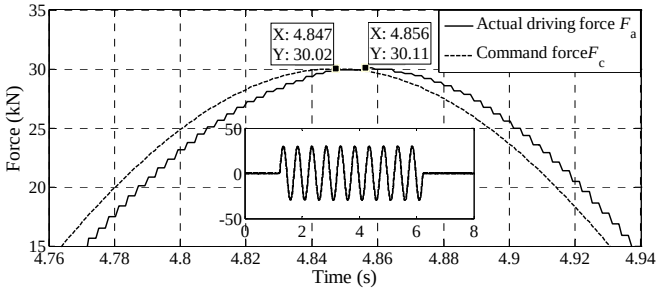

(c) Sinusoidal force case (2 Hz, 30 kN)

Fig. 11 Time delay of the AMD system driven by linear motors

Table 5 Fitting results of the AMD system coefficients

AMD	m_a (kg)	c_{eq} (N·s/m)	F_s (N)
AMD-1	55666.50	4721.66	32.10
AMD-2	56791.76	7788.59	56.45

The dynamic models of AMD subsystems are

AMD-1: $$F_a - 4721.66v + 32.10 = 55666.50a \tag{7}$$

AMD-2: $$F_a - 7788.59v + 56.45 = 56791.76a \tag{8}$$

According to Eqs. (7) and (8), the dynamic models of AMD subsystems are developed in SIMULINK and the open-loop tests have been simulated. The actual driving force records are taken as the inputs in the corresponding simulations. Figs. 12 and 13 show that the simulation results agree well with the test results. Therefore, the dynamic models of AMD-1 and AMD-2 can be used in the design and analysis of AMD control. In the open-loop test case shown in Fig. 13(a), as AMD-1 suffers the velocity limitation at 27.59 s, the velocity of the auxiliary mass is limited by the linear motor driver. To avoid impacting the velocity limitation, the control force in closed-loop is regulated as introduced in the section 3.3 of this paper.

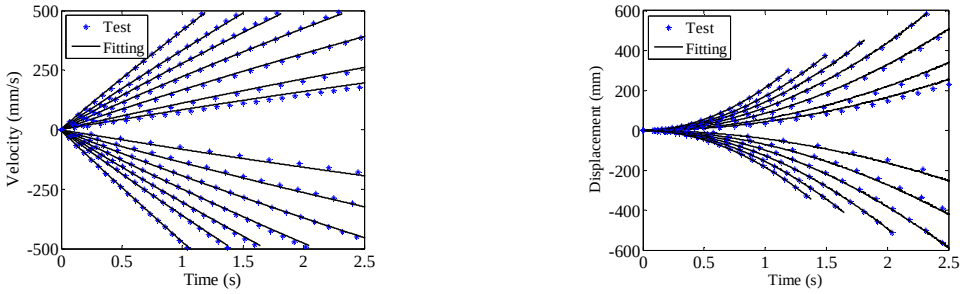

(a) Velocity (b) Displacement

Fig. 12 Fitting results of step force cases with amplitudes range from 1.2 kN to 30 kN (AMD-1)

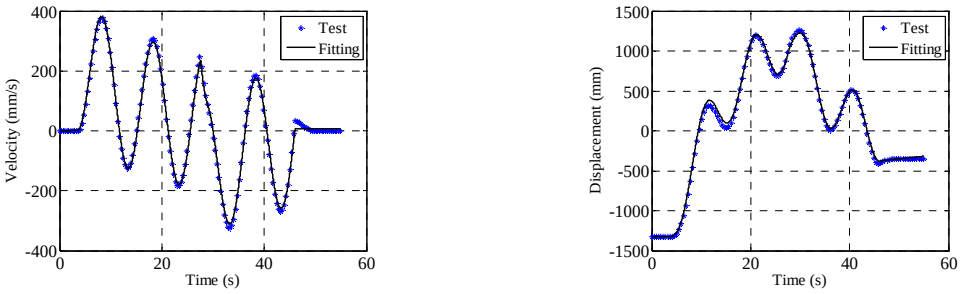

(a) Velocity (b) Displacement

Fig. 13 Fitting results of sinusoidal force case (AMD-1, 0.1 Hz, 8000 N)

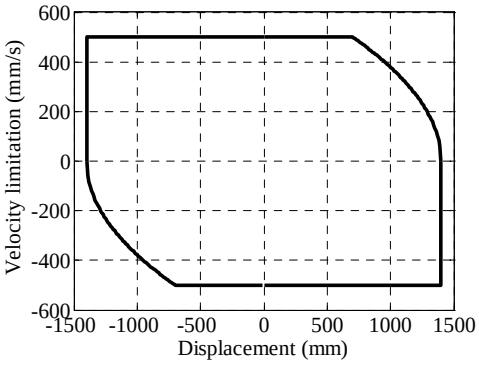

Fig. 14 Relationship between velocity limitation and displacement

3.3 Velocity limitation

As measures to ensure the safety of the system, the velocity limitation has been embedded in the linear motor driver and the bumpers have been installed to limit the stroke of the auxiliary mass. However, the limit forces arranged by the linear motor driver or the reaction forces by the bumpers are uncontrollable, which may make the active control system confused. These uncontrollable limitations can be avoided by regulating the optimal control force in the control strategy.

While the total length of linear guides are 6 m, the length of inertia mass is 2.2 m and the bumpers on both ends of the linear guides occupy 1 m, the effective travel of the AMD subsystem is limited to be ±1.4 m. Simultaneously, the relative velocity of the inertia mass is also limited within the effective stroke range, as shown in Fig. 14: (1) when AMD stroke is within the range [-0.7 m, 0.7 m], the maximum velocity is limited to be less than 0.5 m/s; (2) when AMD exceeds the range [-0.7 m, 0.7 m] and is moving towards the centre of the linear guides, the maximum velocity is also 0.5 m/s; (3) when AMD exceeds the range [-0.7 m, 0.7 m] and is moving away from the centre of the linear guides, the velocity limitation is

$$v_p = v_m \sqrt{\frac{d_m - |d|}{d_m - 0.7}} = v_m \sqrt{2 - 1.42855|d|} \tag{9}$$

where v_m = 0.5 m/s is the maximum velocity limit; d_m = 1.4 m is the maximum displacement limit.

In order to keep the velocity of AMD subsystem always within the velocity limitation (Fig. 14), the optimal control force is regulated by

$$F_{vl} = F_{opt}\left[1 - \left(\frac{v}{v_p}\right)^5\right] \tag{10}$$

where F_{opt} is the optimal control force; F_{vl} is the regulated control force considering the velocity

limitation. The regulated control force F_{vl} is close to the optimal control force F_{opt} in most cases. However, when the velocity of the auxiliary mass comes close to the velocity limitation v_p, the control force is regulated to be very small. Through Eq. (10), the velocity and displacement of inertia mass can be limited smoothly within the safe range.

The rated thrust of the linear motor is 32 kN. However, the maximum driving force is limited to be 30 kN, i.e., when the target force command is larger than 30 kN, only a force of 30 kN can be executed.

3.4 The controller in implementation

The AMD controller is shown in Fig. 15. In AMD control, the control force is determined using variable gain feedback control strategy based on the LQG algorithm. Then the control force is regulated considering the velocity limitation and displacement limitation. The linear motor driver receives control force command from the AMD controller. The PID control algorithm is adopted to regulate the current in the inner-loop control of the linear motor driver.

The controller is developed based on the real-time environment TwinCAT®, which is also the platform of the inner-loop controller of the linear motor. The controller software is based on the discrete-time system with a sampling time of 10 ms. The time taken by each calculation cycle of the control algorithm is about 0.7 ms. As the sampling time of the controller is much less than the self vibration periods of the structure, the effect of time-delay is ignored in this study.

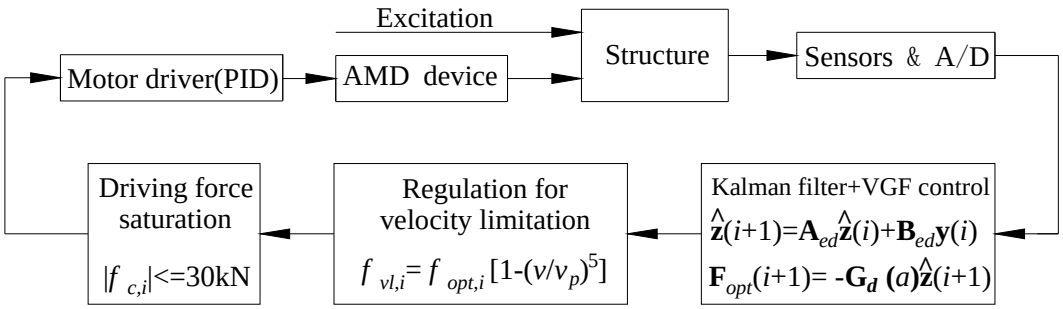

Fig. 15 Diagram of the AMD control system

4. Variable gain feedback control under wind excitations

As the AMD system is installed along the principal X direction, the vibration along principal X direction and the torsional vibration can be suppressed. However, the dynamic response of only one point on each section of the structure is measured. The torsional vibration is still not observable with the feedback subsystem by this study step. So only the control along the principal X direction is considered.

In this study, a continuously variable gain feedback control based on LQG algorithm is adopted to make the AMD system work efficiently within the stroke limitation even under severe strong wind excitations.

4.1 Variable gain feedback control

The equation of motion of the structure with AMD control system is expressed as follows

$$\mathbf{M}_a\ddot{\mathbf{X}} + \mathbf{C}_a\dot{\mathbf{x}} + \mathbf{K}_a\mathbf{X} = \mathbf{P}_w\mathbf{f}_w + \mathbf{P}_u\mathbf{f}_a \tag{11}$$

where $\mathbf{M}_a, \mathbf{C}_a$ and $\mathbf{K}_a$ are the mass matrix, damping matrix and stiffness matrix of the structure-AMD control system, respectively; $\boldsymbol{x} = [x_1, x_2, \cdots, x_n, x_{ra1}, x_{ra2}]^{\mathrm{T}}$ is the displacement vector; $x_i\,(i = 1,2,\cdots,53)$ is the displacement of the i th DOF with respect to the ground; x_{ra1} and x_{ra2} are the displacements of AMD-1 and AMD-2 relative to the floor on which the AMD system located, respectively; $\mathbf{P}_w$ and $\mathbf{P}_u$ denote the acting position matrix of the wind load $\mathbf{f}_w$ and the actual driving force $\mathbf{f}_a$, respectively.

The state-space expression of equation of motion is

$$\begin{aligned} \dot{\mathbf{z}} &= \mathbf{A}_a\mathbf{z} + \mathbf{B}_a\mathbf{f}_a + \mathbf{E}_w\mathbf{f}_w \\ \mathbf{y} &= \mathbf{C}_a\mathbf{z} + \mathbf{D}_a\mathbf{f}_a + \mathbf{E}_{wo}\mathbf{f}_w \end{aligned} \tag{12}$$

where $\mathbf{z}$ is the state vector of the system, $\mathbf{z}(t) = [x_1, x_2, \cdots, x_{53}, \dot{x}_1, \dot{x}_2, \cdots, \dot{x}_{53}, x_{ra1}, x_{ra2}, \dot{x}_{ra1}, \dot{x}_{ra2}]^{\mathrm{T}}$; $\mathbf{y}$ is the measured vector, as shown in Fig. 6 and Table 2; $\mathbf{A}_a, \mathbf{B}_a, \mathbf{C}_a, \mathbf{D}_a, \mathbf{E}_w$ and $\mathbf{E}_{wo}$ are the corresponding coefficient matrices of the system.

To adapt the variation in the intensity level of the wind loads, the quadratic performance function is given as

$$J(\alpha) = \int_0^{\infty}\left[\mathbf{z}^{\mathrm{T}}\mathbf{Q}(\alpha)\mathbf{z} + \mathbf{f}_a^{\mathrm{T}}\mathbf{R}(\alpha)\mathbf{f}_a\right]dt \tag{13}$$

where $\mathbf{Q}(\alpha)$ and $\mathbf{R}(\alpha)$ are the weighting matrix for the state and the weighting matrix for the control force, respectively; α is a scalar variable which indicates the stroke of the auxiliary mass. In this paper

$$\alpha_l = \sqrt{\frac{\sum_{k=l}^{l+n} x_{rak}^2}{n x_{raT}^2}} = \frac{\sigma_l}{x_{raT}} \tag{14}$$

σ_l is the short-term mean-square-deviation, n is the number of the data used to calculate σ_l and x_{raT} is the target value of the auxiliary mass stroke.

The optimal control force $\mathbf{f}_a$ can be obtained by

$$\mathbf{f}_a(t) = \mathbf{G}(\alpha)\hat{\mathbf{z}}(t) \tag{15}$$

where $\mathbf{G}(\alpha)$ can be obtained through LQR algorithm with the weighting matrices $\mathbf{Q}(\alpha)$ and $\mathbf{R}(\alpha)$ by assuming α to be constant with respect to time; $\hat{\mathbf{z}}(t)$ is the state vector estimated with Kalman filter based on the feedback vector $\mathbf{y}$.

The state weighting matrix $\mathbf{Q}(\alpha)$ is partitioned as

$$\mathbf{Q}(\alpha)=\begin{bmatrix} q_s(\alpha)\mathbf{Q}_s^{106\times106} & \mathbf{0}^{106\times4} \\ \mathbf{0}^{4\times106} & q_a(\alpha)\mathbf{Q}_a^{4\times4} \end{bmatrix} \tag{16}$$

where $q_s(a)$ and $q_a(\alpha)$ are scalar functions of α; $\mathbf{Q}_s^{106\times106}$ is the weighting matrix for the displacements and velocities of the structure; $\mathbf{Q}_a^{4\times4}$ is the weighting matrix for the displacements and velocities of the auxiliary masses relative to the floor on which the AMD system is located.

In this study, the scalar functions are given as

$$q_s(\alpha)=c_s\exp\left(\frac{\alpha}{d_s}\right) \qquad q_a(\alpha)=c_a\exp\left(\frac{\alpha}{d_a}\right) \tag{17}$$

where c_s, d_s, c_a and d_a are scalar constants.

Under weak excitations, $q_{s,\max}$ and $q_{a,\min}$, specified with $\alpha_{\min}$, make the capacity of the control system fully utilized. When the intensity of wind is strong, $q_{s,\max}$ and $q_{a,\min}$, specified with $\alpha_{\min}$, restrain the strokes of the auxiliary masses .

In this study, the parameters are given as follows

$$\mathbf{Q}_s=3.5\times10^{-4}\begin{bmatrix}\mathbf{K}_s & \mathbf{0}\\ \mathbf{0} & \mathbf{M}_s\end{bmatrix} \quad \mathbf{Q}_a=\mathrm{diag}([0.2,0.2,2,2]) \quad \mathbf{R}=\begin{bmatrix}1 & 0\\ 0 & 1\end{bmatrix}\times10^{-5}$$

The boundary conditions of $q_s(a)$ and $q_a(\alpha)$ are given by

(1) High control performance: $\alpha_{\min}=0.2, q_{a,\min}=0.001, q_{s,\max}=1$

(2) Restrain the stroke of the auxiliary mass: $\alpha_{\max}=1.41, q_{a,\max}=0.2, q_{s,\min}=0.01$

Then the parameters in Eq. (17) can be calculated to be:

$c_s=2.1351$, $d_s=-0.2637$, $c_a=4.1782\times10^{-4}$, $d_a=0.2292$

The relationship between $q_s(a)$ and $q_a(\alpha)$ is shown in Fig. 16.

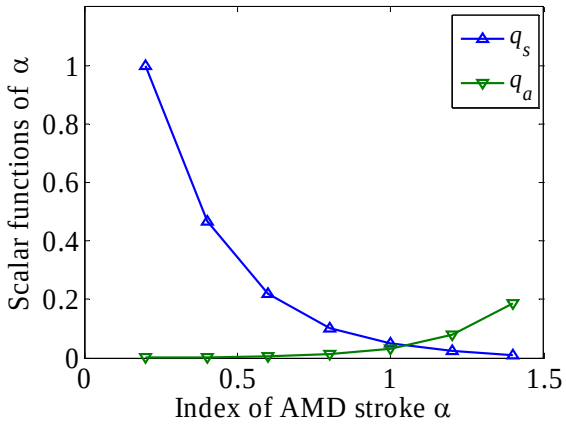

Fig. 16 Scalar functions of performance index

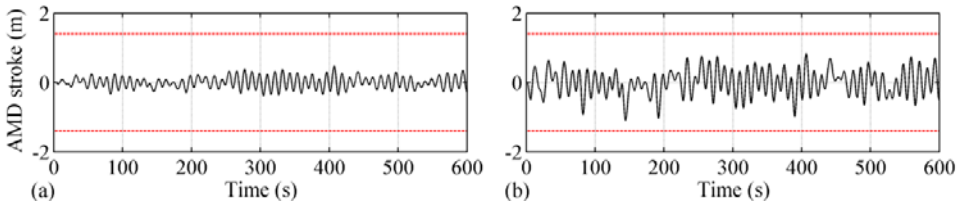

Fig. 17 AMD stroke under wind excitation with 1-year return period: (a) CGF and (b) VGF

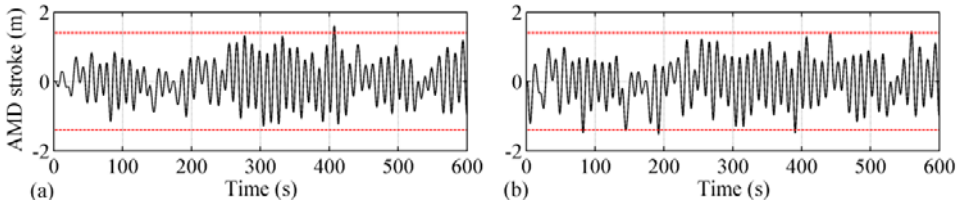

Fig. 18 AMD stroke under wind excitation with 10-year return period: (a) CGF and (b) VGF

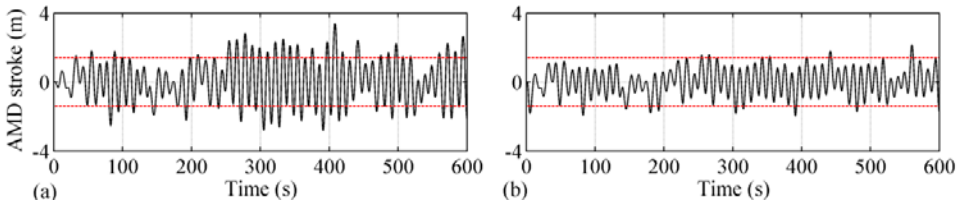

Fig. 19 AMD stroke under wind excitation with 100-year return period: (a) CGF and (b) VGF

4.2 Variable gain feedback control analyses under fluctuating wind excitations

The wind reference pressure at the structure location is 0.24 kN/m^2 with a 10-year return period. Fluctuating wind loads are sampled by white noise filtration method with auto-regressive model. The return periods of the sampled wind loads include 1 year, 10 year and 100 year.

Variable gain feedback (VGF) control analysis of the Canton Tower under the wind excitations with various intensities are carried out. The results of VGF control are compared with that of constant gain feedback (CGF) control. The results are summarized in Table 5. The time-history of the auxiliary mass stroke are shown in Figs. 17-19. The red dashed lines are the stroke limitations (±1.4m) in implementation.

By comparing Figs. 17(a) and 17(b), the stroke of AMD with VGF control is much larger than that with CGF control. The behavior of AMD implies that VGF control works more efficiently than CGF under weak excitations. With respect to the CGF control, the VGF control improves the control effectiveness by 16.33% to the RMS value and by 7.63% to the peak value of the structural displacement (Table 6).

Fig. 18 shows that, the performance of VGF control is equivalent to the CGF control under the wind excitation with a 10-year return period. That is because the constant feedback gain matrix in

CGF control is designed to make the control effectiveness of CGF consistent with that of VGF under the wind excitation with a 10-year return period.

Fig. 19 shows the results under the fluctuating wind load with a 100-year return period. With CGF control, the stroke of the auxiliary mass exceeds the limitation frequently and severely. That implies the auxiliary may impact the bumpers and limiters, even threatens the safety of the system. Thus the AMD with CGF control can not work under strong wind excitations in application. While with VGF control, the AMD works smoothly with the stroke kept within the limitation except few moments. The control effectiveness of VGF decays only 5.4% with respect to the CGF control ignoring the stroke limitation (Table 6).

4.3 control force regulation considering the velocity limitation

Figs. 18(b) and 19(b) show that the stroke of the AMD may exceed the limitation at some moments even with variable gain feedback control. Then the control force regulation given in the section 3.3 of this paper is introduced to restrict the stroke within the limitation. Fig. 20 and Table 6 show the AMD strokes considering the control force regulation presented in section 3.3 (VGF+FR). The AMD strokes are absolutely restricted within the limitation with little loss of the control effectiveness (Table 6).

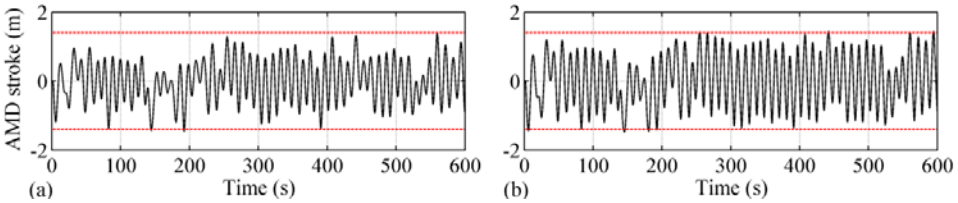

Fig. 20 AMD stroke with VGF considering velocity limitation: (a) 10-year return period and (b) 100-year return period

Table 6 Summarized results of AMD control analysis

	Return period (year)	1			10			100		
	Control strategy	CGF	VGF	VGF +FR	CGF	VGF	VGF +FR	CGF	VGF	VGF +FR
RMS value	x_{37} (without control) (m)	0.049	0.049	0.049	0.169	0.169	0.169	0.366	0.366	0.366
	x_{37} (AMD control) (m)	0.035	0.027	0.027	0.119	0.117	0.118	0.267	0.287	0.291
	x_{ra} of AMD-1 (m)	0.163	0.361	0.359	0.558	0.608	0.594	1.23	0.792	0.727
	f_a of AMD-1 (kN)	2.750	5.521	5.524	9.429	9.830	9.881	20.20	13.42	13.55
Max. value	x_{37} (without control) (m)	0.118	0.118	0.118	0.403	0.403	0.403	0.874	0.874	0.874
	x_{37} (AMD control) (m)	0.092	0.083	0.083	0.314	0.313	0.314	0.717	0.719	0.732
	x_{ra} of AMD-1 (m)	0.468	1.094	1.061	1.605	1.521	1.363	3.418	2.173	1.393
	f_a of AMD-1 (kN)	7.151	15.91	16.58	24.52	26.63	27.58	30	30	30

Note: CGF ---- constant gain feedback control; VGF ---- variable gain feedback control; VGF+FR ---- variable gain feedback control considering the control force regulation presented in section 3.3.

5. Field tests of free vibration control

Field vibration tests of the building are carried out in order to verify the vibration-control performance. The AMD system is adopted as a shaker to excite the structure. Open-loop sinusoidal force excitation, with the amplitude of 3 kN and a frequency of 0.092 Hz, is applied to the structure. The test procedures without control and with AMD control (constant gain feedback control) are listed in Table 7. The time histories of free vibration after excitation are recorded with a sample rate of 50 Hz. Figs. 21-24 show the results of free vibration tests in the principal X direction.

Fig. 21 shows the acceleration of the structure at the height of 438 m. The free vibration attenuation of the structure without control needs a significantly long time because of its low damping. When controlled by AMD system, the vibration of the structure is suppressed to a very low level rapidly. The first-mode damping ratio of the structure increases from 0.35 percent (without control) to 4.1 percent when controlled by AMD system.

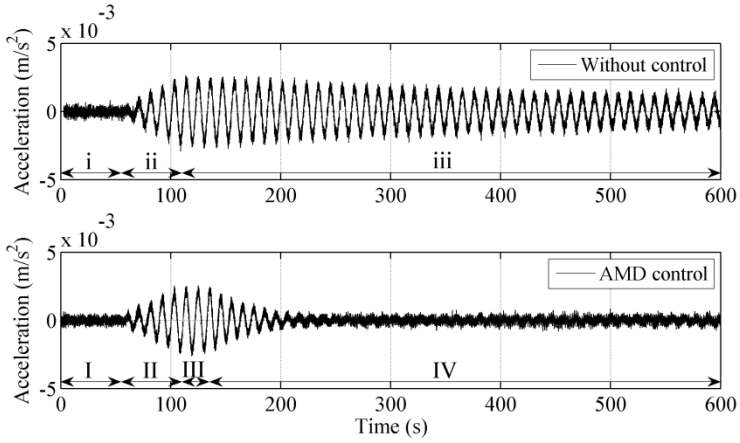

Fig. 21 Acceleration of the structure at the height of 438 m (principal X direction)

Table 7 Phases in test procedures

Free vibration without control	Free vibration controlled by AMD
i. 0-55s: under ambient excitation	I. 0-55s: under ambient excitation
ii. 55s-110s: excited by AMD	II. 55s-110s: excited by AMD
iii. 110s-600s: free vibration attenuation	III. 110s-135s: resetting the AMD system
	IV. 135s-600s: controlled by AMD

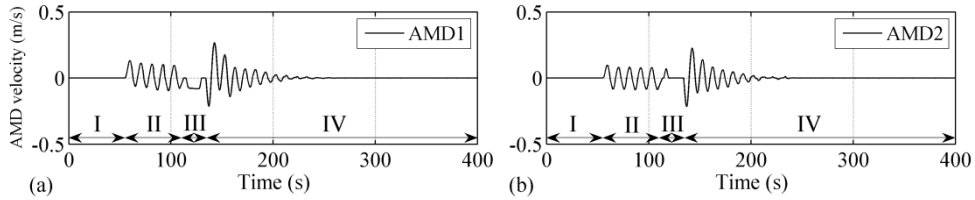

Fig. 22 Relative velocity of AMD subsystems

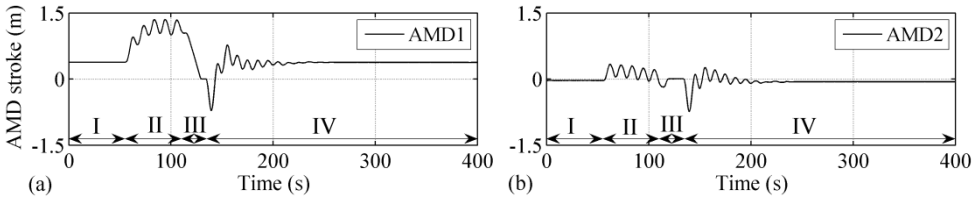

Fig. 23 Relative displacement of AMD subsystems

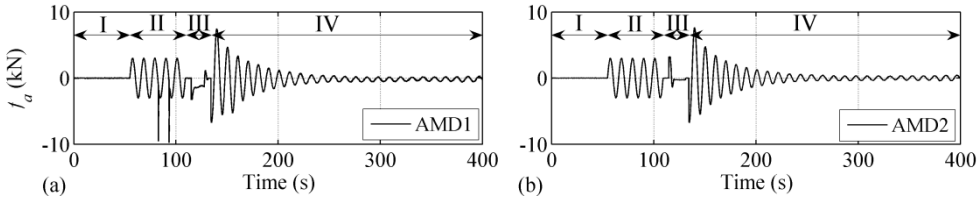

Fig. 24 Actual driving force of the linear motors

Figs. 22 and 23 show the relative velocity and relative displacement of the inertia mass. While in test phase II, the displacement and velocity of AMD are not controlled because the driving force of linear motor is open-loop sinusoidal excitation. The velocity of AMD-1 even reaches the velocity limitation in phase II. When AMD-1 reaches the velocity limitation at 82.73 s and 93.22 s, the driving force of AMD-1 does not execute the target force command but a breaking force programmed in the servo-driver of the linear motor (Fig. 24). As the AMD system is controlled in closed-loop mode in phase IV, the velocity and displacement of AMD are controlled by using LQG algorithm and by considering velocity limitation. Both AMD-1 and AMD-2 run smoothly and effectively in phase IV.

6. Conclusions

This paper has introduced the AMD control for suppressing the wind-induced vibration of the Canton Tower. There are some conclusions drawn from the study: (a) Though the structure is complicated, the structural bending modes are uncoupled in the proposed principal directions. (b) Performance test results confirm the advantages, such as short time delay and long stroke, of the full-scale AMD system driven by linear motors. The time delay of the control force is verified to be less than 10 ms. (c) The numerical simulation results show that, with the VGF control strategy,

the AMD works more efficiently under the weak wind and the auxiliary mass stroke can be kept within its limitation even under the severely strong wind. With respect to the CGF control, the VGF control improves the control effectiveness by 16.33% to the RMS value and by 7.63% to the peak value of the structural displacement. On the other hand, the AMD stroke can be restrained within its limitation even under severe wind excitation with a return period of 100 year. (d) The field tests of free vibration control are carried out. The field test results show that the damping ratio of the first vibration mode increases from 0.35 percent (without control) to 4.1 percent when controlled by AMD system.

Field tests of variable gain feedback control under wind excitations will be carried out next. Fault diagnosis and fault tolerant control will also be developed to make the AMD control system more robust and reliable.

Acknowledgements

This research was supported by the National Science and Technology Support Program (No. 2011BAK02B01) and the National Natural Science Foundation of China (No. 51108143). The authors also acknowledge assistance from Prof. Yi-qing Xiao and Prof. Jun Teng, Shenzhen Graduate School of HIT, for the support in the initial stage of the research. The cooperation of Yan-hui Liu from Guangzhou University and the technical support about the linear motor of Mr. Ming-hua Liu from Han's PME are also acknowledged.

References

Chen, H.P., Tee, K.F. and Ni, Y.Q. (2012), "Mode shape expansion with consideration of analytical modelling errors and modal measurement uncertainty", *Smart Struct. Syst.*, **10**(4-5), 485-499.

Chung, T.T., Cho, S., Yun, C.B. and Sohn, H. (2012), "Finite element model updating of Canton Tower using regularization technique", *Smart Struct. Syst.*, **10**(4-5), 459-470.

Fujita, T., Kamada, T., Masaki, N. and Suizu, Y. (1992), "Active mass damper using multistage rubber bearing and hydraulic actuator", *Proceedings of the Earthquake Engineering 10th World Conference*, Balkema, Rotterdam.

Fujita, T. (2002), "Progress of applications of active vibration control for buildings in Japan", *Prog. Struct. Eng. Mater.*, **4**(4), 353-362.

Hellinger, R. and Mnich, P. (2009), "Linear motor-powered transportation: history, present status, and future outlook", *P. IEEE*, **97**(11), 1892-1900.

Housner, G.W., Bergman, L.A., Caughey, T.K., Chassiakos, A.G., Claus, R.O., Masri, S.F., Skelton, R.E., Soong, T.T., Spencer, B.F. Jr. and Yao, T.P. (1997), "Structural control: past, present, and future", *J. Eng. Mech. - ASCE*, **123**(9), 897-971.

Ikeda, Y., Sasaki, K., Sakamoto, M. and Kobori, T. (2001), "Active mass driver system as the first application of active structural control", *Earthq. Eng. Struct. D.*, **30**(11), 1575-1595.

Lu, X.L., Li, P.Z., Guo, X.Q., Shi, W.X. and Liu, J. (Early view: 2012), "Vibration control using ATMD and site measurements on the Shanghai World Financial Center Tower", *Struct. Des. Tall Spec.* (DOI: 10.1002/tal.1027).

Nagashima, I., Maseki, R., Asarmi, Y., Hirai, J. and Abiru, H. (2001), "Performance of hybrid mass damper system applied to a 36-storey high-rise building", *Earthq. Eng. Struct.D.*, **30**(11), 1615-1637.

Nakamura, Y., Tanaka, K., Nakayama, M. and Fujita, T. (2001), "Hybrid mass dampers using two types of electric servomotors: AC servomotors and linear-induction servomotors", *Earthq. Eng. Struct. D.*, **30**(11),

1719-1743.
Ni, Y.Q., Wong, K.Y. and Xia, Y. (2011), "Health checks through landmark bridges to sky-high structures", *Adv. Struct. Eng.*, **14**(1), 103-119.
Ni, Y.Q., Xia, Y., Liao, W.Y. and Ko, J.M. (2009), "Technology innovation in developing the structural health monitoring system for Guangzhou New TV Tower", *Struct. Control Health Monit.*, **16**(1), 73-98.
Ou, J.P. (2003), *Structural vibration control - active, semi-active and smart control*, Science Press, Beijing, (in Chinese).
Spencer, B.F. Jr. and Nagarajaiah, S. (2003), "Sate of the art of structural control", *J. Struct. Eng. - ASCE*, **129**(7), 845-856.
Yamamoto, M., Aizawa, S., Higashino, M. and Toyama, K. (2001), "Pratical applications of active mass dampers with hydraulic actuator", *Earthq. Eng. Struct. D.*, **30**(11), 1697-1717.